Robotica: page 1 of 17. © Cambridge University Press 2018
doi:10.1017/S0263574718000772

Closed-loop control of bevel-tip needles based on path planning

Benyan Huo†‡*, Xingang Zhao‡, Jianda Han‡ and Weiliang Xu§

†*School of electrical engineering, Zhengzhou University, Zhengzhou, P.R. China*
‡*Shenyang Institute of Automation Chinese Academy of Sciences, Shenyang, P.R. China.*
Emails: zhaoxingang@sia.cn, jdhan@sia.cn
§*University of Auckland, Auckland, New Zealand. Email: p.xu@auckland.ac.nz*

(Accepted July 25, 2018)

SUMMARY
Bevel-tip needles have the potential to improve paracentetic precision and decrease paracentetic traumas. In order to drive bevel-tip needles precisely with the constrains of path length and path dangerousness, we propose a closed-loop control method that only requires the position of the needle tip and can be easily applied in a clinical setting. The control method is based on the path planning method proposed in this paper. To establish the closed-loop control method, a kinematic model of bevel-tip needles is first presented, and the relationship between the puncture path and controlled variables is established. Second, we transform the path planning method into a multi-objective optimization problem, which takes the path error, path length and path dangerousness into account. Multi-objective particle swarm optimization is employed to solve the optimization problem. Then, a control method based on path planning is presented. The current needle tip attitude is essential to plan an insertion path. We analyze two methods to obtain the tip attitude and compare their effects using both simulations and experiments. In the end, simulations and experiments in phantom tissue are executed and analyzed, the results show that our methods have high accuracy and have the ability to deal with the model parameter uncertainty.

KEYWORDS: Medical robotics, Bevel-tip needle, Particle swarm optimization, Path planning, UKF

1. Introduction

Percutaneous punctures are the least invasive surgeries to reach a nidus and are widely performed in biopsy, injection, radio frequency ablation, drug delivery and so on. The clinical efficacy of these surgeries depends heavily on the precision that the puncture needle reaches the desired nidus. However, there are some factors that drive the needle tip to deviate from the desired position, such as tissue inhomogeneity, tissue deformation and surgeon's hand-eye incoordination and fatigue. What's worse, being rigid, the clinical puncture needle is lack of controllability. When the deviation occurs, the only way to revise it is adjusting the needle tail, which would increase the surgery trauma. To improve the controllability of puncture needles, a bevel-tip flexible needle which has a prominent bevel tip and is made up of elastic alloy material has been proposed.[1] While being inserted into tissue, the bevel tip suffers an asymmetric force generated by the tissue deformation, of which the direction can be changed by rotating the needle shaft, as shown in Fig. 1. The force drives the needle to deviate from the puncture direction. That means the bevel-tip needle is more flexible and controllable. Thus, the puncture accuracy can be improved via precise planning and controlling, and nidus blocked by bone, vessel or other sensitive structures can be reached by bevel-tip needles. Due to the complex mechanical interactions between the flexible needle and proteiform tissue, it is difficult to model and

* Corresponding author. E-mail: huoby@zzu.edu.cn

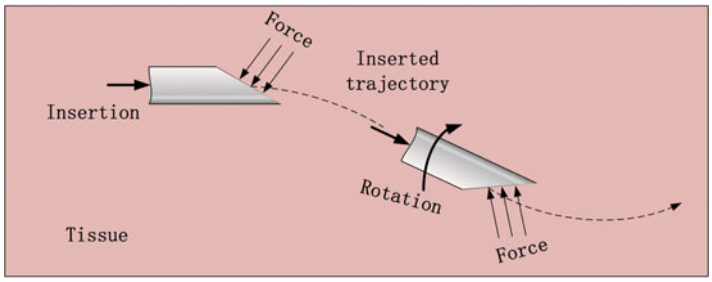

Fig. 1. The steering process sketch of bevel-tip needles.

drive bevel-tip needles using existed robotics-based algorithms and devices. In this paper, we focus on the whole driving system and research the model, path planning and control methods of bevel-tip needles.

To drive the flexible needle precisely, dynamic and kinematic models of flexible needles have been developed. Dynamic models focus on the analysis of needle tip cutting force and the modeling of tip deflection. Because the needle tip is too tiny to mount a force sensor, the cutting force is obtained indirectly via two methods, modeling the cutting force directly[2,3] and subtracting the modeled friction of needle body from the whole needle suffered force which is measured by a force sensor mounted on the needle tail.[4,5] The tip deflection models are mainly based on the cantilever beam model,[6,7] segmented cantilever beam model[8] and spring-beam-damping model.[9] However, dynamic models are very complex and remain in theoretical analysis. The kinematic model, bicycle model,[1] was established via analyzing the needle tip motion and the model parameters were recognized via experimental datum. Wooram *et al.*[10] went further to simplify the model by decreasing the model parameters from three to one. The kinematic model is directly based on experimental datum and hides the complexity of the interaction between the flexible needle and the flexible biological tissue. This leads to a concise kinematic model which is widely employed in puncture path planning methods and driving methods. However, existed research works did not explain how the nonlinear kinematics model was employed. In our work, the kinematics model is analyzed further and is described in insertion-length domain rather than time domain.

Being inserted into tissue, the bevel-tip needle deviates from the puncture direction. That means the insertion trajectory is not a simple straight line. It is essential to plan a path to guide the inserting process. Due to the nonholonomic constrain of the kinematic model, traditional path planning methods are unsuitable for bevel-tip needles. Some path planning methods designed for bevel-tip needles have been proposed. The path planning problem is first researched in 2D plane. Alterovitz *et al.*[11,12] turned the path planning in 2D plane into a nonlinear optimization problem via finite element model and random Markova process, respectively, and got the optimized puncture path by minimizing the object function. Zhang *et al.*[13] connected the initial point and the nidus with straight lines and arcs, and found the best path via calculating the cost function of different combinations of lines and arcs. Huo *et al.*[14] researched the path planning method in nonhomogeneous tissue via dynamic programming, in which the initial attitude of the needle tip was optimized for the first time. The methods in 2D plane are based on the discretization of the workspace or the insertion path. The number of discrete states increases sharply when those methods are expanded from 2D plane to 3D space and the cost time of searching for the best solution in the large number of states is unacceptable. To reduce the time complexity, rapidly exploring random tree (RRT)[15] was employed. Some improvements were proposed based on the RRT algorithm, such as introducing a reachability-guided sampling heuristic method to accelerate RRT algorithm,[16] executing RRT algorithm many times to compute a large number of randomized paths and from which the best one was selected.[17] Though the RRT algorithm can generate an obstacle-avoidance path, it cannot find the best or the next best solution. That is why the work was executed in ref. [18]. Wang *et al.*[19] selected several obstacle-avoidance 2D planes connecting the initial point and the target, then employed the path planning method designed for 2D plane. Thus, the complex path planning problem in 3D space was simplified. However, a key question that how to select the 2D planes was not presented. Duindam *et al.*[20] proposed a semi-automated 3D path planning method using inverse kinematics and analyzed the reachability. To deal with obstacles, users had to select one or more intermediate poses, which needed technique and experience. Another

question is that most path planning methods are verified only via simulations. In view of existing problems, we propose a new path planning method that takes the path length, path error and path dangerousness into account and verify it via experiments.

The purpose of path planning is guiding the process of steering the bevel-tip needle to a target precisely. There are three different kinds of methods to realize this purpose. The first kind of methods is calculating a control action directly according to the current state of the needle tip and the target, such as sliding mode control,[21] reachable-region control,[22] duty-cycling control.[23] Those methods have an obvious disadvantage that cannot deal with obstacles. The second kind of method is based on path planning. This is the mainly method used in current works[24,25] due to the convenience of extending from path planning methods. And we also adopt this method in our work. The third method is path tracking control which is not appear in current works.

No matter which method mentioned above relies on the current information of the needle tip. Obviously, the simple and direct way is installing a sensor on the needle tip. This way obtains the position and attitude directly and precisely. However, it is almost impossible due to the tiny needle tip. Most existent position and attitude sensors are too large to install on the tiny tip. Though existing a little enough magnetic sensor, it is a great quantity of work to remould the needle and the work environment since that the sensor requires no magnetic material existing in its workplace. We focus on how to obtain the position and attitude angle of flexible needles via existent equipment. Several devices are able to image biological tissue, such as ultrasound, computed tomography and magnetic resonance imaging. These devices also image the puncture needle in tissue. Thus, we can get the tip position via existent equipment. As attitude angle cannot be measured via images for the same reason that the needle tip is tiny, the remain question is how to obtain attitude angle. There are two existent methods, approximation method[26] and estimation method proposed in our early work.[22,27] In this paper, we analyze and compare the two methods via simulations and experiments.

In this paper, we focus on the path plan method and the steering method. Our contributions are summarized as following. The kinematics model is analyzed further and described in insertion-length domain rather than time domain. We propose a new path planning method which takes the path length, path error and path dangerousness into account and employ this method in the steering process. We also analyze and compare the estimation and approximation methods of the attitude angle via simulations and experiments for the first time. The article is organized as following. In Section 2, the kinematic model of the bevel-tip needle is presented and analyzed. Section 3 presents the path planning method in detail. The steering method is discussed in Section 4. Section 5 presents the simulation results, experimental setup and experiment results. Finally, Section 6 presents conclusions and the possible future work.

2. Kinematic Model of the Bevel-Tip Needle

Refer to ref. [16], a simplified kinematic model of the bevel-tip needle is built based on the following assumptions.

1. Tissue is homogeneous and undeformed.
2. The flexible needle is stiffness in axial direction. Thus, the tip orientation follows the needle tail exactly.
3. The needle body follows the tip exactly, and the needle position does not change in radial direction after being inserted into tissue.

Under those assumptions, the bevel-tip needle follows an arc when driven in tissue. In the following of this section, we first present the kinematic model in time domain, and then transform it into insert-length domain.

As shown in Fig. 2, the curvature of the arc followed by bevel-tip needles is κ. At the needle tail, the insertion speed is υ and the rotation speed is ω. The tip position and attitude angle in the world coordinate system Ψ_ω is $\boldsymbol{q}^\omega = [\,x\ y\ z\ \alpha\ \beta\ \gamma\,]$, α, β, γ are Euler angles that the needle tip rotates around x, y, z axes, respectively.

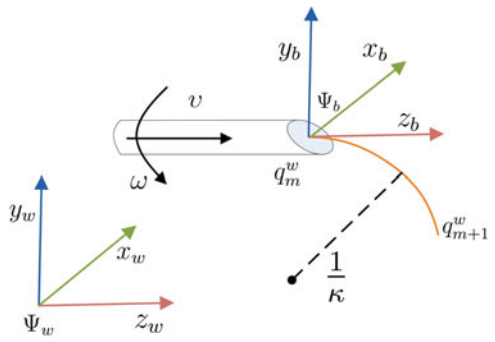

Fig. 2. The kinematic model of bevel-tip needles.

Then, we get the kinematic model of flexible needles: (The detail of modeling process could be found in ref. [16].)

$$\dot{\boldsymbol{q}} = \boldsymbol{A}(\boldsymbol{q}) \begin{bmatrix} \upsilon \\ \omega \end{bmatrix} = \begin{bmatrix} \sin\beta & 0 \\ -\cos\beta\sin\alpha & 0 \\ \cos\alpha\cos\beta & 0 \\ \kappa\cos\gamma\sec\beta & 0 \\ \kappa\sin\gamma & 0 \\ -\kappa\cos\gamma\tan\beta & 1 \end{bmatrix} \begin{bmatrix} \upsilon \\ \omega \end{bmatrix}, \tag{1}$$

where the attitude angle β is not equal $n\pi + \frac{\pi}{2}, n \in \mathbb{N}$ to keep the kinematic model nonsingular.

As shown in (1), the kinematic model is strongly nonlinear and the model states are coupling with the inputs. The model is also nonholonomic because the needle tip position cannot be integrated from the velocity directly. It is impossible to linearize the model or to transform it to standard state space equations. Therefore, we discretize (1) as following:

$$\boldsymbol{q}_{i+1} = \boldsymbol{q}_i + \boldsymbol{A}(\boldsymbol{q}_i) \begin{bmatrix} \upsilon_i \\ \omega_i \end{bmatrix} \Delta T, \tag{2}$$

where $i = 0, 1, 2, \ldots$ is the time step.

According to assumption 3, the needle position remains unchanged in radial direction after being inserted into tissue. The assumption means that states of the flexible needle are frozen when the insertion process is stopped. Thus, we can pause the insertion process to correct the path inserting error or ensure that the insertion process is safe without worrying about the real-time problem. Duindam *et al.*[28] assumed that the insertion trajectory had no connection with the insertion velocity and angular velocity, which will hold in homogeneous, relatively stiff phantom tissue. As our current algorithms are verified in the phantom tissue, we follow this assumption. This assumption may fail in biological tissue which is proteiform and inhomogeneous. We will not consider this situation in this work and leave it to the future research. Therefore, the insertion length and rotation angle are employed rather than the velocities in the insertion process. Then, the kinematic model is rewrite as $\boldsymbol{q}_{i+1} = \boldsymbol{q}_i + \boldsymbol{A}(\boldsymbol{q}_i)[\, l_i \;\phi_i \,]^T$, where l_i and ϕ_i are the insertion length and rotation angle in the i th step. To simplify the kinematic model, the control variables are split into $[\, 0 \;\phi_i \,]^T$ and $[\, l_i \;0 \,]^T$, namely rotation control and insertion control. According to (1), the rotation control only affects the state γ and the needle tip will follow an arc whose center position is constant and whose radius is $1/\kappa$ when the insertion control is executed. Thus, the kinematics model is transformed from time domain to insertion-length domain. The above analysis makes the description of the needle's movement more clear. The path planning method proposed in the next section is exactly based on this analysis.

3. Path Planning Method

In this section, we describe the path planning problem as an optimization problem and adopt multi-objective particle swarm optimization method (MPSO) to solve the problem. First, the mathematical

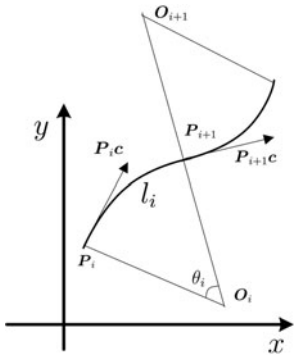

Fig. 3. Relationship between the insertion path and the control sequence.

description of the planned path is set up based on geometric principle. Second, mathematical formulations of three optimization objectives are given. At last, the solving process of the optimization problem is presented.

3.1. Relationship between control variables and the insertion path

According to the discrete kinematic model of flexible needles $\boldsymbol{q}_{i+1} = \boldsymbol{q}_i + \boldsymbol{A}(\boldsymbol{q}_i)[\, l_i \;\phi_i \,]^T$, an insertion path can be described certainly and uniquely by a control sequence $[\,(l_1; \phi_1), (l_2; \phi_2), \ldots, (l_n; \phi_n)\,]$. The common path planning methods first generate paths without consideration of feasibility and then adjust those paths according to the model constrains. Due to the nonlinear and nonholonomic model of flexible needles, the adjustment will take a lot of efforts. Thus, we plan the control sequence corresponding to a feasible path instead of planning the insertion path. To reduce the control sequence length without accuracy loss, the insertion process is dealt with based on geometric constraints that the rotation control only affects the state γ and the needle tip will follow an arc. In this manner, l_i is any value greater than 0. In the following, we set up the relationship between the planned path and the control sequence based on geometric principle. The relationship is analyzed in 2D plane first and then extended to 3D space.

A segment of insertion path in 2D is shown in Fig. 3. The segment consists of two arcs corresponding to two insertion controls. An arc can be uniquely determined by $(\boldsymbol{P}_i, \boldsymbol{P}_i\boldsymbol{c}, \boldsymbol{O}_i, l_i)$. Here, $\boldsymbol{P}_i$ is the start point of the arc, $\boldsymbol{P}_i\boldsymbol{c}$ is the unit tangent vector of the arc at $\boldsymbol{P}_i$, $\boldsymbol{O}_i$ is the center of the arc, l_i is the insertion length. We can get the end point $\boldsymbol{P}_{i+1}$ and the tangent vector $\boldsymbol{P}_{i+1}\boldsymbol{c}$ of the arc at $\boldsymbol{P}_{i+1}$ as following. Then, the tangent vector $\boldsymbol{P}_{i+1}\boldsymbol{c}$ is unitized, $\boldsymbol{P}_{i+1}\boldsymbol{c} := \frac{\boldsymbol{P}_{i+1}\boldsymbol{c}}{|\boldsymbol{P}_{i+1}\boldsymbol{c}|}$.

$$\begin{aligned} \theta_i &= \kappa l_i \\ \boldsymbol{P}_{i+1} &= \boldsymbol{P}_i \cos\theta_i + (1-\cos\theta_i)\,\boldsymbol{O}_i + \tfrac{1}{\kappa}\boldsymbol{P}_i c \sin\boldsymbol{\theta_i} \\ \boldsymbol{P}_{i+1}c &= (1-\cos\theta_i)\,\boldsymbol{O}_i + \boldsymbol{P}_{i+1}\cos\theta_i - \boldsymbol{P}_i \end{aligned} \tag{3}$$

As mentioned above, the rotation control only affects the state γ. Thus, the center of the arc is changed when the rotation control is executed. In 2D plane, the rotation angle can only be π. Due to the arc center $\boldsymbol{O}_{i+1}$ is symmetric with $\boldsymbol{O}_i$ about $\boldsymbol{P}_{i+1}$, the position of $\boldsymbol{O}_{i+1}$ is

$$\boldsymbol{O}_{i+1} = 2\boldsymbol{P}_{i+1} - \boldsymbol{O}_i. \tag{4}$$

Equations (3) and (4) are the iterative relationship between the insertion path and the control variables in 2D plane. The two equations make up a model of the bevel-tip needle in the view of geometry. The whole planned path in 2D can be obtained according to the control sequence and the two equations. Extended to 3D space, an arc also can be determined by $(\boldsymbol{P}_i, \boldsymbol{P}_i\boldsymbol{c}, \boldsymbol{O}_i, l_i)$, and the equation to get the end point $\boldsymbol{P}_{i+1}$ of the arc is the same as (3), except that all variables are three dimensional. As the rotation angle is not constant, Eq. (4) is not suitable for the 3D space. According to the space geometry, a vector $\boldsymbol{P}$ rotates Φ around a unit vector $\boldsymbol{A}$, the new vector after rotated is $\boldsymbol{P'} = \boldsymbol{P}\cos\Phi + \boldsymbol{A} \times \boldsymbol{P}\sin\Phi + \boldsymbol{A}(\boldsymbol{A}^*\boldsymbol{P})(1-\cos\Phi)$.

To calculate $\boldsymbol{O}_{i+1}$, two auxiliary vectors are introduced, $\boldsymbol{P}_{\text{oc1}} = \boldsymbol{O}_i - \boldsymbol{P}_{i+1}$ and $\boldsymbol{P}_{\text{oc2}} = \boldsymbol{O}_{i+1} - \boldsymbol{P}_{i+1}$. The vectors are substituted into the space vector rotation formula and the result is

$$\begin{aligned} \boldsymbol{P}_{\text{oc1}} &= \boldsymbol{O}_i - \boldsymbol{P}_{i+1} \\ \boldsymbol{P}_{\text{oc2}} = \boldsymbol{P}_{\text{oc1}} \cos\phi_{i+1} &+ \boldsymbol{P}_{i+1}c \times \boldsymbol{P}_{\text{oc1}} \sin\phi_{i+1} + \boldsymbol{P}_{i+1}c\,(\boldsymbol{P}_{i+1}\boldsymbol{c}^{*}\boldsymbol{P}_{\text{oc1}})\,(1 - \cos\phi_{i+1}), \\ \boldsymbol{O}_{i+1} &= \boldsymbol{P}_{\text{oc2}} + \boldsymbol{P}_{i+1} \end{aligned} \tag{5}$$

where ϕ_{i+1} is the rotation angle, and $\boldsymbol{P}_{i+1}\boldsymbol{c}$ is the unit tangent vector at $\boldsymbol{P}_{i+1}$.

Thus, we set up the relationship between the insertion path and the control sequence in 3D space.

3.2. Optimization functions

The best path has following characters: reaching the target precisely, short length and avoiding obstacles. Thus, optimization objectives are the path error $f_{\text{tipErr}}(\boldsymbol{\Theta})$, namely the distance between the end of planned path and the target, the path length $f_l(\boldsymbol{\Theta})$ and the path dangerousness $f_d(\boldsymbol{\Theta})$ caused by obstacles, where $\boldsymbol{\Theta} = [\,(l_1; \phi_1), (l_2; \phi_2), \ldots, (l_n; \phi_n)\,]$ is a control sequence. The optimization function of the path planning method is

$$\min f\,(\boldsymbol{\Theta}) = \left[f_{\text{tipErr}}\,(\boldsymbol{\Theta})\,, f_l\,(\boldsymbol{\Theta})\,, f_d\,(\boldsymbol{\Theta})\right] \tag{6}$$

In the following, the three optimization objectives are presents in detail.

3.2.1. Path error. A path is determined by a control sequence uniquely. Thus, the endpoint of a path is calculated by (3) and (5) according to the corresponding control sequence. We define the endpoint of a path as $\boldsymbol{P}_{\text{tip}}(\boldsymbol{\Theta})$. The path error is the distance between the endpoint and the target:

$$f_{\text{tipErr}}\,(\boldsymbol{\Theta}) = \left|\boldsymbol{P}_{\text{tip}}\,(\boldsymbol{\Theta}) - \boldsymbol{P}_d\right|, \tag{7}$$

where $\boldsymbol{P}_d$ is the target.

3.2.2. Path length. The whole length of a path is the sum of all l_i in a control sequence. Therefore, the path length is

$$f_l\,(\boldsymbol{\Theta}) = \sum_{i=1}^{n} l_i \tag{8}$$

3.2.3. Path dangerousness. The planned path should avoid obstacles such as blood vessel, nerve and bone. Moreover, it is better to reserve a safe distance D to ensure the needle will not pass through obstacles. Thus, we define the dangerousness caused by a single obstacle as following:

$$f_o\,(d) = \begin{cases} +\infty & \text{if} \quad d < D \\ \frac{KD}{d} & \text{if} \quad d \geq D \end{cases}, \tag{9}$$

where d is the minimum distance between an obstacle and the planned path, K is the weight coefficient.Multiple obstacles may exist in the treatment area. The path dangerousness function is established by summing up the dangerousness shown in (9):

$$f_d\,(\boldsymbol{\Theta}) = \sum_{1}^{m} f_{oj}\left(d_j\right), \tag{10}$$

where m is the number of obstacles.

In the following, the calculating method of the minimum distance d is presented. Also, the method is analyzed in 2D plane first, and then extended to 3D space. To simplify the distance calculating process, obstacles are surrounded by circles. The distance between an obstacle and the path is replaced by the distance between the circle surrounding the obstacle and the path. As shown in Fig. 4, an irregular obstacle is surrounded by a circle fitly. Some definitions are given as following. $\boldsymbol{O}_j^b$ is the center of the circle surrounding the j th obstacle, whose radius is r_j. d_{ji} is the minimum distance between the

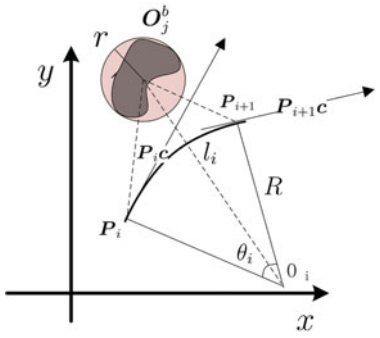

Fig. 4. Obstacle in 2D plane.

j th circle and the i th arc, and $d_j = \min_{i=1}^{n} d_{ji}$. L_{ji} is the distance between $\boldsymbol{O}_j^b$ and the center of the i th arc, $L_{ji} = |\boldsymbol{O}_j^b - \boldsymbol{O}_i|$. Let, $s_1 = \boldsymbol{P}_{ob1} * \boldsymbol{P}_i\boldsymbol{c}$ and $s_2 = \boldsymbol{P}_{ob2} * \boldsymbol{P}_{i+1}\boldsymbol{c}$, where $\boldsymbol{P}_{ob1}, \boldsymbol{P}_{ob2}$ are vectors from $\boldsymbol{P}_i, \boldsymbol{P}_{i+1}$ to $\boldsymbol{O}_j^b$, respectively. The minimum distance d_{ji} relates to signs of s_1, s_2 as following, which can be proved by geometric methods.

$$d_j = \min_i d_{ji} = \min_i \begin{cases} \left|L_{ji} - \frac{1}{\kappa}\right| - r & \text{if } s_1 \geq 0, s_2 \leq 0 \\ \min\left(\left|\boldsymbol{O}_j^b - \boldsymbol{P}_{i+1}\right|, \left|\boldsymbol{O}_j^b - \boldsymbol{P}_i\right|\right) - r_j & \text{otherwise} \end{cases} \tag{11}$$

Then, we extend this formula from 2D to 3D space. Definitions and analyzing process mentioned above are suitable for 3D space. There is only one difference that the line connecting $\boldsymbol{O}_j^b$ and $\boldsymbol{O}_i$ may not be in the plane that contains the arc and $\boldsymbol{O}_i$. Hence, the computational method of d_{ji} should be modified when $s_1 \geq 0, s_2 \leq 0$. The nearest point to the obstacle is the intersection of the arc and the projection of the line crossing $\boldsymbol{O}_j^b$ and $\boldsymbol{O}_i$ on the plane containing the arc. The computational formula is $d_{ji} = \sqrt{(L_{ji}^2 + \frac{1}{\kappa^2} - \frac{2}{\kappa} L_{ji}\cos\varphi)} - r_j$ where $\varphi = \arcsin|\frac{\boldsymbol{O}_o * (\boldsymbol{P}_i\boldsymbol{c} \times \boldsymbol{P}_{i+1}\boldsymbol{c})}{|\boldsymbol{O}_o||\boldsymbol{P}_i\boldsymbol{c} \times \boldsymbol{P}_{i+1}\boldsymbol{c}|}|$ is the included angle between the vector $\boldsymbol{O}_o = \boldsymbol{O}_i - \boldsymbol{O}_j^b$ and the plane containing the arc. Thus, the formula of the distance d_j in 3D space is

$$d_j = \min_i d_{ji} = \min_i \begin{cases} \sqrt{L_{ji}^2 + \frac{1}{\kappa^2} - \frac{2}{\kappa} L_{ji}\cos\varphi} - r_j & \text{if } \quad s_1 \geq 0, s_2 \leq 0 \\ \min\left(\left|\boldsymbol{O}_j^b - \boldsymbol{P}_{i+1}\right|, \left|\boldsymbol{O}_j^b - \boldsymbol{P}_i\right|\right) - r_j & \text{otherwise} \end{cases} \tag{12}$$

Using (9), (10) and (12), the path dangerousness in 3D space is obtained.

3.3. Optimization method

The optimization objectives are (7), (8) and (10), representing the path error, path length and path dangerousness, respectively. According to the form of those equations, we know that the optimization objectives are iterative and nonlinear. General algorithms, such as lagrangian multiplier method, gradient method and Newton method, are not suitable for this problem. In this article, MPSO is employed. There are several different multi-objective PSO methods,[25] such as composite weighting multi-objective PSO, multi-objective PSO based on pareto method and dynamic weighting multi-objective PSO which is used in our work.

There are three optimization objectives: path error $f_{\text{tipErr}}(\boldsymbol{\Theta})$, path length $f_l(\boldsymbol{\Theta})$ and path dangerousness $f_d(\boldsymbol{\Theta})$. The last objective keeps the path away from obstacles. If any obstacles stay in the safe distance D of a path, the path is invalid. Obviously, this objective has no connection with other objectives. While, path length and path error are conflicting. Let D_{id} be the distance between the initial point and the target. When $\min f_l(\boldsymbol{\Theta}) = 0$, there is $f_{\text{tipErr}}(\boldsymbol{\Theta}) = D_{\text{id}}$. When $\min f_{\text{tipErr}}(\boldsymbol{\Theta}) = 0$, there could be multiple discrete $f_l(\boldsymbol{\Theta})$, and $f_l(\boldsymbol{\Theta}) > D_{\text{id}}$. That means, there are many local minimum solutions of this optimization. To avoid local minimums, we relax path error $f_{\text{tipErr}}(\boldsymbol{\Theta})$ during the early phase and focus on the optimization of path length $f_l(\boldsymbol{\Theta})$. With the decreasing of path length, the optimization of path error is strengthened. Thus, we get the weighting function of dynamic weighting

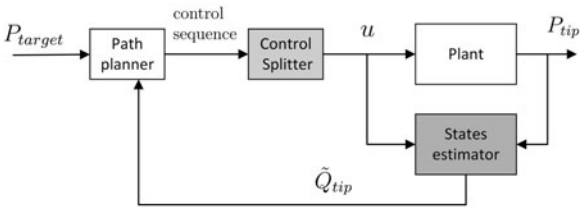

Fig. 5. Closed-loop control system diagram.

multi-objective PSO algorithm:

$$\min f(\mathbf{\Theta}) = \min \left\{ K_t f_{\text{tipErr}}(\mathbf{\Theta}) + K_l f_l(\mathbf{\Theta}) + f_d(\mathbf{\Theta}) \right\}, \tag{13}$$

where $K_t = \frac{C_t}{|f_l(\Theta) - C_L| + 1}$ and $K_l = C_l |f_l(\Theta) - C_L|$ are dynamic weighting coefficients about path length, C_t, C_l, C_L are invariant coefficients and tuned according to the offline simulations results.

The optimization process in our work is the standard PSO process. The followings are the optimization steps:

1. Initiating the particle swarm Q, the number of Q is n_Q maximum iteration times is I_Q. Set every particle's position Q_i and velocity V_i randomly.
2. Calculating every particle's adaptive value. $f_{\text{tipErr}}(\mathbf{\Theta})$, $f_l(\mathbf{\Theta})$, $f_d(\mathbf{\Theta})$ are obtained according to (7), (8) and (10), respectively. The adaptive value is obtained by (13).
3. Going through the particle swarm, recording every particle's position Q_i^b when the adaptive value is individual best and the position Q_g^b of the best global particle.
4. Updating every particle's velocity and position: $V_i^k = \omega_k V_i^{k-1} + c_1 r_1 (Q_i^b - Q_i^{k-1}) + c_2 r_2 (Q_g^b - Q_g^{k-1})$, $Q_i^k = Q_i^{k-1} + V_i^k$. Here, k is the iterative step. ω_k is the inertia weight coefficient. c_1, c_2 are learning factors. r_1, r_2 are random values.
5. Checking whether the end condition is reached. If reached, the algorithm is ended; the optimized path and the corresponding control sequence $\mathbf{\Theta}$ are obtained. Otherwise, the algorithm is continuing.

4. Steering Method

Obtaining the optimized path and the corresponding control sequence $\mathbf{\Theta}$ is the first step to complete an insertion surgery. In this section, we analyze the second step, namely how to steer a bevel-tip needle to a target precisely. The corresponding control sequence can be utilized to drive the bevel-tip needle. The needle will follow the planned path and reach the target precisely in ideal environment which is obviously nonexistent. Due to the tissue heterogeneity and the complex mechanical interactions between the flexible needle and proteiform tissue, the kinematic model parameter identified off-line may be different from the actual value, and the needle tip, target and obstacles may slide in the insertion process due to tissue deformation. To overcome error and indeterminacy, the closed-loop feedback control is necessary. Figure 5 presents the control flow as follow: (1) A control sequence is generated by the path planner according to the target and the feedback of the current needle tip states. (2) The sequence is split and employed to drive the bevel-tip needle. (3) The needle tip is located and compared with the desired trajectory. (4) If the needle tip deviates from the desired trajectory, the control flow goes to step 1. Otherwise, the control flow goes to step 2. This closed loop continues until the needle tip reaches the target. The path planner employs the path plan method mentioned above. There are two new modules in the Fig. 5, control splitter module and state estimator module. The following explains why we introduce the two modules.

4.1. Control splitter

As mentioned in Section 3.1, the control sequence is $[(l_1; \phi_1), (l_2; \phi_2), \ldots, (l_n; \phi_n)]$ and the value of l_i, $i = 1, 2, \ldots, n$ is arbitrary value greater than 0. If we use the control sequence directly, the position error of the needle tip may accumulate too large to be corrected. To correct tip error immediately, we introduce the control splitter which will divide l_i into a number of constant L_c, namely the insertion

step length. The rotation control ϕ_i is also separated with the insertion control variable. Thus, a $(l_i; \phi_i)$ is separated into executed sequence $[\,(0; \phi_i), (l_{i1}; 0), (l_{i2}; 0), \ldots, (l_{nN_i}; 0)\,]$, where $l_{i1} = l_{i2} = \ldots = l_{nN_{i-1}} = L_c$, $0 < l_{nN_i} \leq L_c$ and $\sum_{j=1}^{N_i} l_{ij} = l_i$. The first and second control pairs of the executed sequence are used to steer the needle.

4.2. States estimator

States estimator estimates attitude angles according to the measured position of the needle tip. There are two existent methods, approximation method and estimation method. In the following, we present and analyze the two methods.

4.2.1. Attitude approximation method. The approximation method was proposed by Adebar.[26] In our work, we go further to explain why this method is valid and the application range.

The kinematic model of flexible needles is shown in (1). Here, we focus on the attitude angles and extract attitude equations as following.

$$\begin{bmatrix} \dot{\alpha} \\ \dot{\beta} \\ \dot{\gamma} \end{bmatrix} = \begin{bmatrix} \kappa \cos\gamma \sec\beta * \upsilon \\ \kappa \sin\gamma * \upsilon \\ -\kappa \cos\gamma \tan\beta * \upsilon + \omega \end{bmatrix} \tag{14}$$

The value of κ is affected by characters of the bevel-tip needle, such as material, diameter, angle of bevel-tip and characters of tissue such as density, elasticity and composition. In different literatures, κ is different, but most of them range between $1/50\text{mm}^{-1}$ and $1/500\text{mm}^{-1}$. All κ are very small. Thus, we can approximate attitude angles as (15). Via the approximation, three attitude angles are reduced to one and γ can be obtained by simply accumulating the input rotation angles.

$$\begin{bmatrix} \dot{\tilde{\alpha}} \\ \dot{\tilde{\beta}} \\ \dot{\tilde{\gamma}} \end{bmatrix} = \begin{bmatrix} 0 \\ 0 \\ \omega \end{bmatrix} \tag{15}$$

Thus, we can infer that the approximate error increases along with κ increasing and this method cannot deal with the effect of noise. As we cannot get the true value of attitude angles, simulations are executed to verify our inference in next section.

4.2.2. Attitude estimation method. Another kind of methods to get unmeasurable states is estimation methods. Due to the strong nonlinearity of the kinematic model as shown in (1), the unscented kalman filter (UKF) is employed to estimate attitude angles. The algorithm process in our work is the same as the general UKF process. Therefore, the detail of UKF algorithm is not presented. The same as approximation method, simulations are executed in the next section to verify the effect of UKF.

5. Simulations and Experiments

In this section, the proposed methods are verified via simulations first, including states estimator and path planning method. Then, the experiment platform is introduced, including the platform setup, needle tip located method and the model parameter identification. At last, experiments are performed and results are analyzed.

5.1. Simulations of states estimator

The simulation parameters are set as follows: the standard deviation of measurement noise and process noise are 0.15 mm and 0.01 radian; The control sequence is [(100, 0)], namely inserting a needle 100 mm without rotation. The attitude angle approximation error Att_e and the estimation error Est_e are defined as $\sqrt{(\alpha - \tilde{\alpha})^2 + (\beta - \tilde{\beta})^2 + (\gamma - \tilde{\gamma})^2}$. Simulations are executed with different model parameter κ which ranges between $1/50\ \text{mm}^{-1}$ and $1/500\ \text{mm}^{-1}$. As shown in Fig. 6, simulation results verify that the approximate error increases along with κ increasing. When κ is less than $1/200\ \text{mm}^{-1}$, the effect of noise surpasses the model parameter's effect and the order of κ is chaotic. This phenomenon verifies the approximation method cannot deal with the effect of noise. When κ is constant, attitude error Att_e is accumulated along with the insertion length. This is due to the simplex

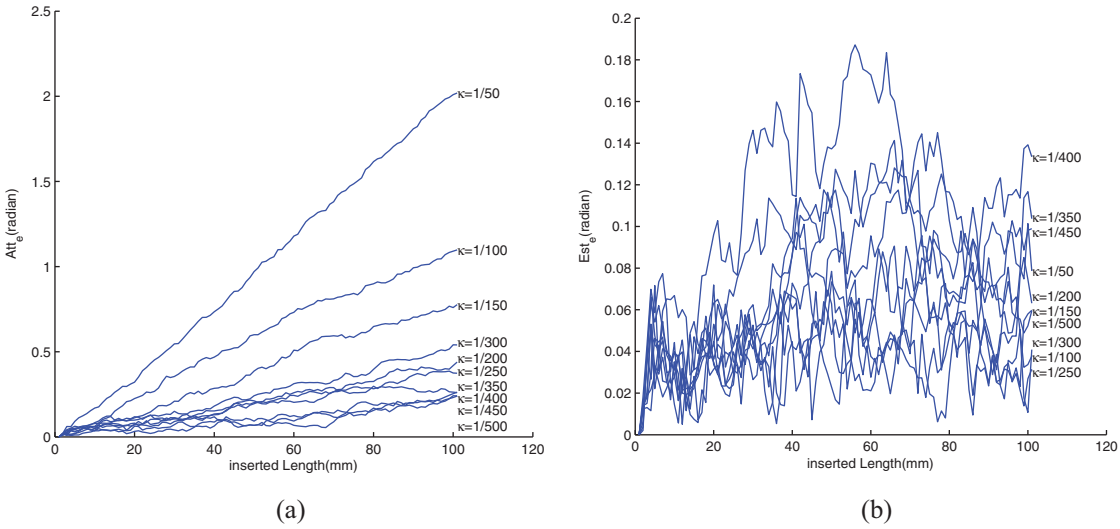

(a) (b)

Fig. 6. Att_e (a) and Est_e (b) of the approximation method under different model parameters κ. (Note: Fig. 6(a) and (b) have different scales on y-axis.). (a) Approximation error Att_e. (b) Estimation error Est_e.

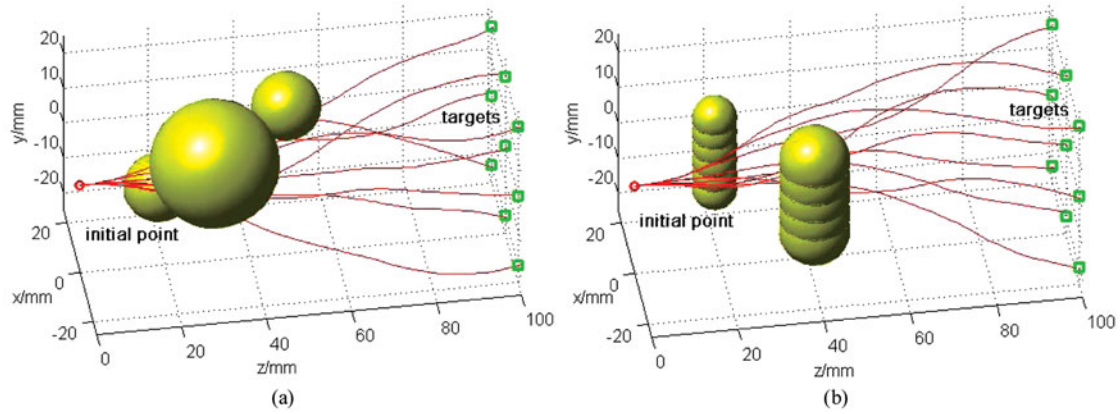

Fig. 7. Simulation results of path planning algorithm in different workspaces. (a) Workspace 1. (b) Workspace 2.

control sequence. If there are rotation controls in the control sequence, Att_e maybe reduce when the rotation control is executed. This can be explained according to (14). If the control sequence is simplex, the attitude angle γ changes slowly. Thus, $\dot{\alpha}$, $\dot{\beta}$, $\dot{\gamma}$ will keep positive or negative in a wide range of insertion length and Att_e will increase. However, the control sequence contains rotation control, γ sharp changes when rotation control is executed. The sign of $\dot{\alpha}$, $\dot{\beta}$, $\dot{\gamma}$ may change and this may lead Att_e to decrease. That is to say Att_e is less than the error shown in Fig. 6(a) in practical experiments. Most of Est_e is under 0.1 radian and is much smaller than Att_e. Compared with the approximation method, the order of κ is totally chaotic in Fig 6(b). The reason is that the main influence factor of the estimation method precision is noise rather than the model parameter κ. What's more, Est_e remains at a small error steadily when rotation controls exist in the control sequence, on the contrary Att_e is unstable. This phenomenon can be confirmed via simulations, but we do not exhibit the simulation results due to the similarity with results shown in Fig. 6(b). In a word, the estimation method is more robust and precise than the approximation method. Though the computation complexity of estimation method is higher, it is acceptable to be used in states estimation of the flexible needle.

5.2. Simulations of path planning method

As shown in Fig. 7, two complex workspaces with obstacles are set up to verify the effect of proposed path planning method. While in experiments, we focus on the precision of our driving method and the workspace is simple and without obstacles. The two workspaces are set up as following. Workspace 1

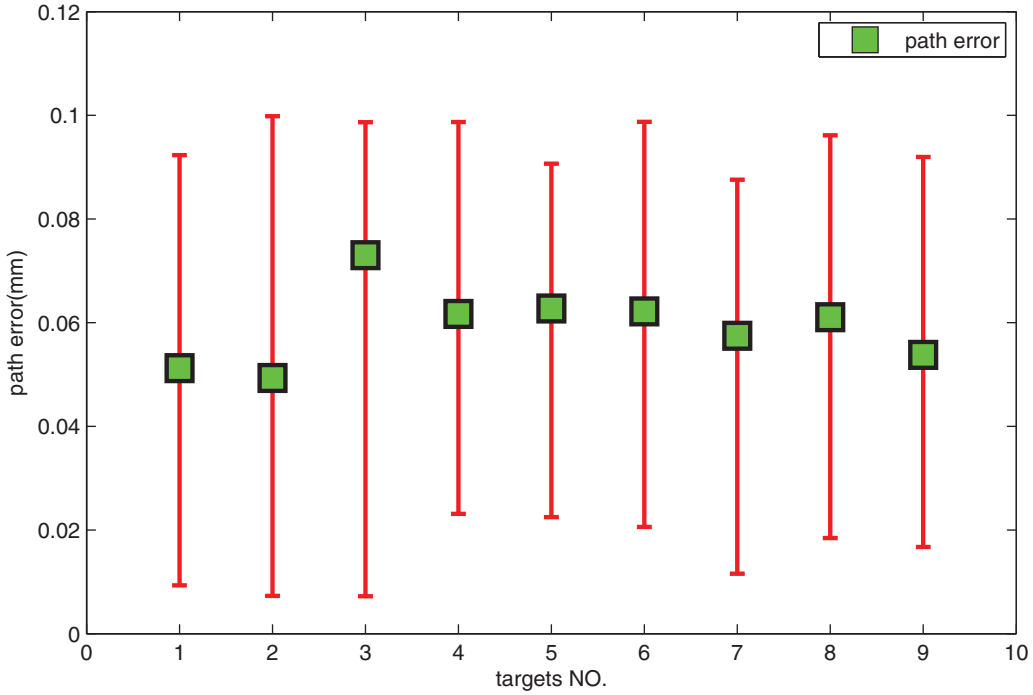

Fig. 8. Statistics of simulated path errors for workspace 1.

includes three sphere obstacles to estimate discrete regions of sensitive tissue. Workspace 2 includes two columnar obstacles to estimate blood vessels or bones which cannot be punctured. To deal with obstacles in the same way, we cover sphere obstacles and columnar obstacles with spheres. Sphere obstacles are covered by single sphere, and columnar obstacles are covered by multiple spheres which are overlapping to cover the obstacle closely and completely. The initial point is the origin point of the coordinate system, and targets are symmetric in the plane which depth is 100 mm. The workspaces are shown in Fig. 7, in which red circles are initial points, green squares are targets and yellow spheres are obstacles.

The model parameter κ is decided by the needle material, diameter, bevel tip angle and tissue characters. κ is recognized off-line in experiments and set to be 0.02 mm^{-1} in simulations. The parameters of multiple partial swarm optimization method are set as follows: the population is $n_Q = 50$, the number of maximum iterations is $I_{\max} = 1000$, inertia weight coefficient is $\omega_k \in [0.5, 1.5]$, learning factors are $c_1 = 1$, $c_2 = 2$. The stop conditions of the algorithm are the iterative time reaches the maximum iterations or path error that the distance between the end of a path and a target is less than 0.1 mm. If the path error is still larger than 0.1 mm when the algorithm ends, the path planning method fails.

Simulations are performed in conditions mentioned above. Results of simulations are shown in Fig. 7 in which red lines represent the planned paths. According to the figure, we know that the planned paths reach targets precisely. Simulations are performed 10 times, respectively, for targets in the workspace 1. Simulation results are recorded and shown in Fig. 8 in which the abscissa axis represents different targets and the ordinate axis represents the mean and value range of simulated path errors. Due to PSO algorithm is a stochastic optimization method, path errors are not constant. We get that the mean of path errors stays in the range [0.05,0.08] mm and the path errors are less than 0.1 mm. Ninety simulation results, namely ten results for nine targets, respectively, prove that the proposed path planning method is effective. The path error is quite small due to that the simulation conditions are ideal. Figure 9 shows convergence processes of path length and path error in one simulation trial. The path length converges quickly as shown in Fig. 9(a), while the path error converges slower than the path length does as shown in Fig. 9(b). The results conform to the analysis of the path planning method in Section 3.3. When the method ends, the path error is 0.082 mm and the iteration times is 587.

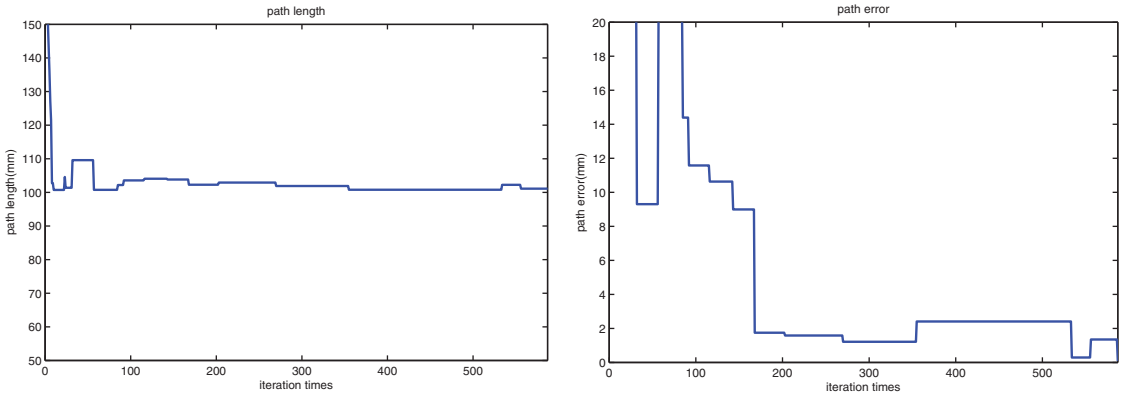

Fig. 9. Convergence process of the path planning method. (a) Convergence process of the path length; (b) Convergence process of the path error.

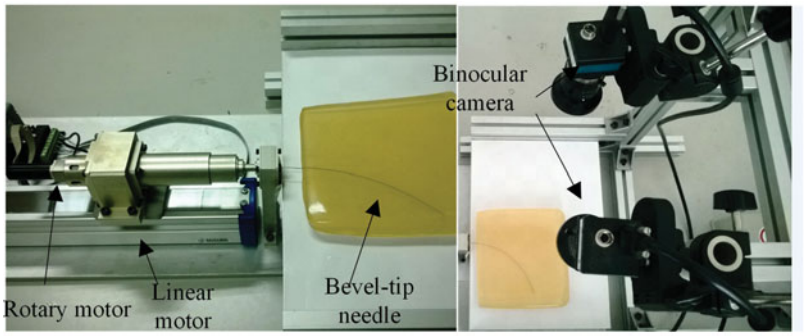

Fig. 10. The steering platform of flexible needles, including a rotary motor, a linear motor and two cameras.

The simulation results prove that the proposed method can deal with different targets and workspaces.

5.3. Experiment platform

To verify proposed methods, an experiment platform is needed to execute experiments. We use a kind of transparent material made of gelatin and carrageenan, instead of biological tissue. And binocular vision, instead of medical image, is employed to locate the needle tip position. Thus, we simplify the experiment environment and focus our work on the verification of proposed methods. In the following of this section, the platform is presented first, and then the needle tip located method is introduced.

5.3.1. Platform setup. The platform is designed according to the kinematic characters. As shown in Fig. 10, the platform includes a rotary motor (FAULHABER Inc.), a linear motor (MISUMI Inc.) and two cameras (Imagingsource Inc.). The rotary motor is a DC motor and is used to execute the rotation control. The linear motor pushes the flexible needle into tissue. The motors are controlled by their respective drive controllers that implement position and speed closed-loop control internally. Hence, we regard the motor drive controller as a module whose transfer function is 1. The control commands are sent to motor drive controllers directly and are assumed to be executed immediately without any deviation. The two cameras constitute a binocular visual system to locate the needle tip in 3D space. The binocular visual system only provides the position information of the needle tip. Thus, it can be replaced by other locating methods such as position sensors and medical imaging systems, without revising other parts of the steering system. The experimental tissue should be transparent due to the visual locating system. We confect the transparent tissue with 12% gelatin and 1% carrageenan. The homogeneity of gelatin tissue allows us to study the proposed method without the complication of biological tissue. The flexible needle is made up of Ni–Ti alloy with a bevel angle of 30° and a diameter of 0.8 mm. All experiments are performed on this platform.

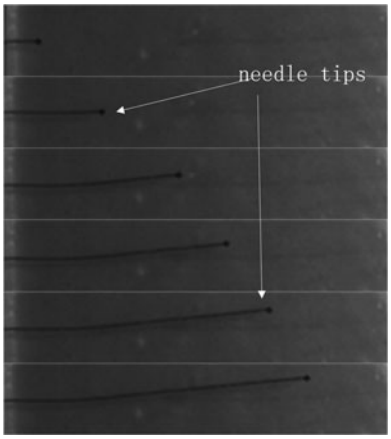

Fig. 11. The needle tip located results in gelatin tissue.

5.3.2. Needle tip located method. In this part, we focus on how to locate the needle tip. As shown in Fig. 10, cameras look downward the gelatin tissue almost vertically. Light coming from the needle tip passes through the gelatin tissue, goes into air and reaches cameras. There is a refraction in the light path. Here, we ignore the refraction error on account of three reasons. One reason is that the incidence and emergence angle are close to zero; the optical path in gelatin tissue is short; the positions of initial point, the needle tip and the target are relative to the initial position of the needle tip in gelatin tissue. Thus, we regard the located position as the actual position of the needle tip. The locating process is as following.

The resolution of cameras is 2592×1944, and the field of view is close to the A4 paper size, namely 297×210 mm^2. The pixel position of needle tip in one image is located by matching image features of needle tip. Obviously, searching needle tip in the whole image is a waste of time. As the trajectory of needle tip is continual, we search the current needle tip around the last needle tip position. Figure 11 is shown the needle tip located results. The tip position in 3D space is calculated via the needle tip pixel positions in images captured by the two cameras and the internal and external camera parameters calibrated according to ref. [29]. Positions used in the driving system are relative. That means the initial position of needle tip is zero and other positions, such as positions of the target, the current needle tip and obstacles, are relative to the initial position. Thus, we only pay attention to the repeated measurement accuracy of the stereo-vision system. Keeping the needle tip unchanged and measuring 242 times, we get the repeated measurement data of the needle tip position that includes three independent components. Standard deviations are 0.12 mm, 0.03 mm and 0.12 mm, respectively, for three components of the measurement data. The distribution of repeated measurements around the mean value approximates to normal distribution. Thus, we regard the measurement uncertainty as an effect of Gaussian noise. The standard deviations of noises are the same as the repeated measurement data.

5.4. Experiments of steering method

In this section, needle driving experiments based on path planning method are performed on the platform mentioned above. In simulations, the model parameter is set to be large to test the effect of path planning method. But we have to recognize the model parameter in experiments. Thus, we introduce the parameter recognition first.

5.4.1. Kinematic model parameter recognition. The model parameter κ is recognized via the method mentioned in ref. [1]. Actually, the recognized parameter is the radius of the insertion trajectory rather than κ, which is the reciprocal of the radius. The flexible needle is inserted into gelatin tissue without rotatory control five times sequentially. Recognized results are shown in Table I from which we know that values of radius are variable. The difference may be caused by the phantom tissue's temperature, non-homogeneous or both. The mean value of recognized results is used in our experiments. That is $\kappa = 1/284.37$ mm^{-1}. As the model parameter used in path planning method and the state estimator may be different from the actual value, experiments are affected by the model parameter uncertainly.

Table I. Model parameter κ recognized results.

Trials	1	2	3	4	5
Radius (mm)	285.97	282.86	296.45	258.67	297.90

Table II. Steering precision of experiments.

Targets (mm)	OLC* (mm)	CLCA* (mm)	CLCE* (mm)
[0 0 100]	2.75	0.36	0.44
[0 12 100]	4.86	0.75	1.00
[0 -12 100]	4.89	2.55	1.56
[5 0 100]	5.42	1.15	0.42
[5 12 100]	1.97	2.79	0.87
[5 -12 100]	4.13	1.89	0.99
[-5 0 100]	3.62	4.19	0.40
[-5 12 100]	2.15	2.38	1.15
[-5 -12 100]	1.04	3.90	0.44
Mean	3.43	2.22	0.81

*OLC:Open-loop control; CLCA:Closed-loop control with attitude approximation method; CLCE:Closed-loop control with attitude estimation method.

And experiment results prove the robustness of proposed methods, including path planning method, state estimator and the whole control system.

5.4.2. Results of steering experiments. In this paper, we present a path planning method which is validated via simulations in Section 5.2, a steering method based on the proposed path planning method and two attitude-obtaining methods which are analyzed according to simulation results. Those methods work together to steer the flexible needle. So, we evaluate those methods as a whole. To validate two attitude-obtaining methods, we couple the two methods with the path planning method and the steering method, respectively. Thus, three kinds of experiments are performed in our work. The first kind is open-loop control of which the control diagram is as shown in Fig. 5 without feedback; another kind is closed-loop control with attitude approximation method; the last kind is closed-loop control with attitude estimation method. The first kind is regard as a control group. The evaluation criterion is whether the needle tip reaches specified targets or not.

The coordinates of the initial needle tip are chosen to be the world coordinates in which nine targets are specified. The needle tip position is rebuilt in the stereo-vision coordinates and is transformed to the world coordinates. There is no obstacle in the workspace due to that obstacles may have different effects on the steering precision of nine different targets. So, we exclude the effects of obstacles and focus on the steering precision. In the open-loop control process, a path is plan previously and the corresponding control series is executed to steer the flexible needle. There is no on-line correction of the control series. While in the closed-loop control process, the control series is corrected by the path planning method according to the current needle tip position and attitude angle. The length of control step is 5 mm, that means the insertion path and control series are corrected when the needle tip moves forward 5 mm. Obviously, along with the decrease of the control period, the number of path planning and the time of steering process increase. The control process is ended when the distance between the needle tip and the target is less than 0.1 mm or the needle tip exceeds the target.

In each kind of experiments, nine insertions are performed for nine targets, insertion trajectories and steering precisions are recorded. There are 27 insertions totally. Results are shown in Table II. The mean values are 3.43 mm, 2.22 mm and 0.81 mm, respectively, for the three kinds of experiments. Insertion errors of open-loop control experiments are biggest and various that means there are model parameter error and phantom tissue uncertainty. Closed-loop control reduces the insertion errors sharply, that proves the proposed steering system is effective for steering the flexible needle. The attitude estimation method is more effective than the attitude approximation method due to that not only the mean value but also all the insertion errors of the closed-loop control with attitude estimation method are smaller. As analysis in Section 4.2, the approximation method is also acceptable when

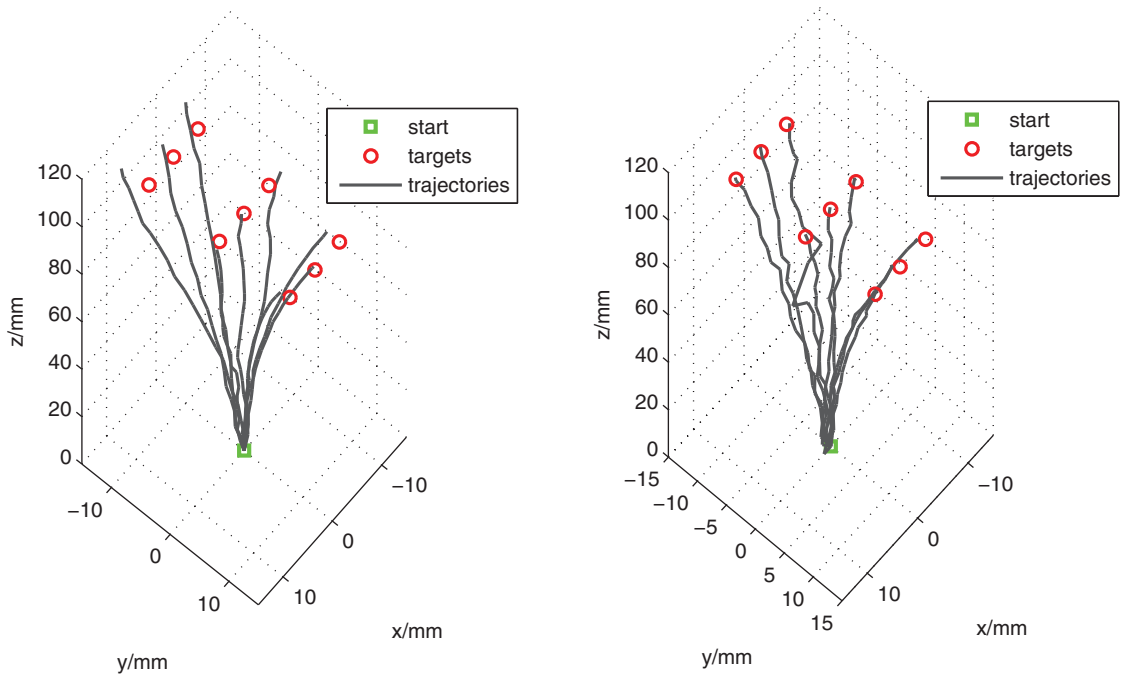

Fig. 12. Insertion trajectories in phantom tissue. Red circles represent targets. (Note: To present insertion trajectories clearly, Fig. 12 has different scale on z-axis compared to x-axis and y-axis). (a) Insertion trajectories with CLCA method. (b) Insertion trajectories with CLCE method.

the model parameter κ is small. Thus, the attitude approximation method can be employed in suitable case. Insertion trajectories of closed-loop control are shown in Fig. 12. Repeated experiment is also performed. We execute five insertions of which the target is $[0, -12, 100]$ mm for the two closed-loop control methods, respectively. The mean values of the steering precision are 2.80 mm and 0.92 mm.

5.4.3. Analysis of experiment results and application in biological tissue. Those experiments are performed in phantom tissue which is assumed to be homogeneous and undeformed as assumptions in Section 2. However, the handmade phantom tissue cannot be absolutely homogeneous, and existing inhomogeneous will affect the steering process and precision. Due to the unknowable homogeneous, the steering results are variable even for the same target.

In the open-loop control experiments, errors of preplanned paths are less than 0.1 mm, while errors of insertion paths are various from 1.04 mm to 5.42 mm. Due to the model parameter error and phantom tissue uncertainty, the needle tip errors arise and accumulate variously. In the CLCA method, the estimation of attitude angles is accumulated by the rotation angle at the end of the needle. Thus, the estimation results may diverge from the truth values that are affected by the model parameter error and phantom tissue uncertainty. Due to the wrong attitude angles, the new planned path may not reach the target, and the closed-loop control could not revise the path error. As a result, CLCA method reduces the path errors slightly and the errors are various from 0.36 mm to 4.19 mm. In the CLCE method, the estimation of attitude angles is very precise. Thus, the closed-loop control can revise the path error properly and the errors are reduced sharply. However, the number of rotation controls increases. The rotation of needle tip will incise the phantom tissue and release the stress of the bent needle shaft, which will drive the needle tip to diverge from its original trajectory. That is why the insertion trajectories of CLCE method are not smooth. The results prove that CLCE method is robust even when the assumptions are not satisfied.

In the current work, experiments are performed in phantom tissue whose characteristics are similar to the assumptions. Now, we analyze problems that may occur in biological tissue which is more complex, viscous, elastic and inhomogeneous. Due to the viscidity, assumption 2 is not satisfied. Thus, the angle of the needle tip may lag behind the needle tail's. Some researchers have analyzed

this situation and built up a torsional dynamics model.[30] This model is proposed to integrate the flexible needle model. Due to the elasticity and heterogeneity, assumptions 1 and 3 are not satisfied, which means the model parameter will change dramatically and deformed tissue will alter the position of needle's shaft and tip. To steering the flexible needle accurately, the heterogeneity and elasticity of biological tissue should be taken into account, which will increase the complexity of the path planning method and the steering method. As a consequence, steering a flexible needle in biological tissue accurately is more complex than in phantom tissue and we leave the challenges for the future.

6. Conclusion

In this paper, we propose a path planning method, a steering method and analyze two attitude-obtaining methods. Those methods are validated via simulations and experiments in phantom tissue. Results indicate that the path planning method and steering method are effective and robust, the attitude estimation method works better than the approximation method. The advantages of the proposed path planning method are taking the path length, path error and path dangerousness into account and obtaining a control series corresponding with the planned path at the same time. And the control sequences can be employed to steer the flexible needle directly. The steering method is based on the path planning method and only needs the needle tip position that can be obtained by the clinical equipment such as computed tomography and ultrasound. That means the steering method reduces the design complexity of the bevel-tip needle due to the unnecessary of a sensor on the needle tip. Thus, the steering method is conveniently extended to the clinical setting in the future. The disadvantage of the steering method is that the path planning method should be executed many times in one insertion, which can be solved by introduce a path tracking method. In the current work, experiments are performed in phantom tissue which will be replaced by biological tissue in the future. And the stereo-vision system will be replaced by computed tomography or Ultrasound.

Acknowledgements

This work is partially supported by the Nation Natural Science Foundation of China (61473265) and the Science and Technology Innovation Research Team Support Plan of Henan Province (17IRTSTHN013).

References

1. R. Webster, N. Cowan, G. Chirikjian and A. Okamura, *Nonholonomic Modeling of Needle Steering* (Springer, Berlin-Heidelberg, 2006), vol. **21**, pp. 35–44.
2. S. Misra, K. Reed, B. Schafer, K. Ramesh and A. Okamura, "Mechanics of flexible needles robotically steered through soft tissue," *Int. J. Robot. Res.* **29**(13), 1640–1660 (2010).
3. D. Wei, H. Han and Z. J. Du, "The Tip Interface Mechanics Modeling of a Bevel-Tip Flexible Needle Insertion," *International Conference on Mechatronics and Automation* (2012) pp. 581–586.
4. R. J. Roesthuis, Y. R. J. van Veen, A. Jahya and S. Misra, "Mechanics of Needle-Tissue Interaction," *International Conference on Intelligent Robots and Systems* (2011) pp. 2557–2563.
5. A. Asadian, R. V. Patel and M. R. Kermani, "A Distributed Model for Needle-Tissue Friction in Percutaneous Interventions," *IEEE International Conference on Robotics and Automation* (2011) pp. 1896–1901.
6. A. Asadian, M. R. Kermani and R. V. Patel, "An Analytical Model for Deflection of Flexible Needles During Needle Insertion," *IEEE/RSJ International Conference on Intelligent Robots and Systems* (2011) pp. 2551–2556.
7. M. Abayazid, R. J. Roesthuis, R. Reilink and S. Misra, "Integrating deflection models and image feedback for real-time flexible needle steering," *IEEE Trans. Robot.* **29**(2), 542–553 (2013).
8. A. Haddadi and K. Hashtrudi-Zaad, "Development of a Dynamic Model for Bevel-Tip Flexible Needle Insertion into Soft Tissues," *IEEE International Conference on Engineering in Medicine and Biology Society* (2011) pp. 7478–7482.
9. K. G. Yan, T. Podder, Y. Yan, I. L. Tien, C. W. S. Cheng and N. Wansing, "Flexible needle-tissue interaction modeling with depth-varying mean parameter: Preliminary study," *IEEE Trans. Biomed. Eng.* **56**(2), 255–262 (2009).
10. P. Wooram, K. Jin Seob, Z. Yu, N. J. Cowan, A. M. Okamura and G. S. Chirikjian, "Diffusion-Based Motion Planning for a Nonholonomic Flexible Needle Model," *IEEE International Conference on Robotics and Automation* (2005) pp. 4600–4605.
11. R. Alterovitz, A. Lim, K. Goldberg, G. S. Chirikjian and A. M. Okamura, "Steering Flexible Needles Under Markov Motion Uncertainty," *IEEE/RSJ International Conference on Intelligent Robots and Systems* (2005) pp. 1570–1575.

12. R. Alterovitz, K. Goldberg and A. Okamura, "Planning for Steerable Bevel-tip Needle Insertion Through 2D Soft Tissue with Obstacles," *Proceedings of the 2005 IEEE International Conference on Robotics and Automation* (2005) pp. 1640–1645.
13. Y. Zhang, Y. Zhao and C. Hao, "2D path planning of bevel tip flexible needle in soft tissue," *Robot* **33**(6), 750–757 (2011).
14. B. Huo, X. Zhao, J. Han and W. Xu, "Motion Planning for Flexible Needle in Multilayer Tissue Environment with Obstacles," *IEEE International Conference on Systems, Man, and Cybernetics* (2012) pp. 3292–3297.
15. J. Xu, D. Vincent, A. Ron and G. Ken, "Motion Planning for Steerable Needles in 3D environments with Obstacles Using Rapidly-Exploring Random Trees and Backchaining," *IEEE International Conference on Automation Science and Engineering* (2008) pp. 41–46.
16. S. Patil and R. Alterovitz, "Interactive Motion Planning for Steerable Needles in 3D Environments with Obstacles," *International Conference on Biomedical Robotics and Biomechatronics* (2010) pp. 893–899.
17. S. Patil, J. Burgner, R. J. Webster and R. Alterovitz, "Needle steering in 3-D via rapid replanning," *IEEE Trans. Robot.* **30**(4), 853–864 (2014).
18. F. Liu, A. Garriga-Casanovas, R. Secoli and F. R. y. Baena, "Fast and adaptive fractal tree-based path planning for programmable bevel tip steerable needles," *IEEE Robot. Autom. Lett.* **1**(2), 601–608 (2016).
19. J. Wang, X. Li, J. Zheng and D. Sun, "Dynamic path planning for inserting a steerable needle into a soft tissue," *IEEE/ASME Trans. Mechatronics* **19**(2), 549–558 (2014).
20. V. Duindam, R. Alterovitz, S. Sastry and K. Goldberg, "Three-dimensional motion planning algorithms for steerable needles using inverse kinematics," *Int. J. Robot. Res.* **29**(7), 789–800 (2010).
21. D. C. Rucker, J. Das, H. B. Gilbert, P. J. Swaney, M. I. Miga, N. Sarkar and R. J. Webster, "Sliding mode control of steerable needles," *IEEE Trans. Robot.* **29**(5), 1289–1299 (2013).
22. B. Y. Huo, X. G. Zhao, J. D. Han and W. L. Xu, "A control method of flexible needle puncture control based on reachable decision," *Control Theory & Appl*. **31**(10), 1423–1430 (2014).
23. A. Krupa, "A New Duty-Cycling Approach for 3D Needle Steering Allowing the Use of the Classical Visual Servoing Framework for Targeting Tasks," *International Conference on Biomedical Robotics and Biomechatronics* (2014) pp. 301–307.
24. M. C. Bernardes, B. V. Adorno, P. Poignet and G. A. Borges, "Robot-assisted automatic insertion of steerable needles with closed-loop imaging feedback and intraoperative trajectory replanning," *Mechatronics* **23**(6), 630–645 (2013).
25. G. Vrooijink, M. Abayazid, S. Patil, R. Alterovitz and S. Misra, "Needle path planning and steering in a three-dimensional non-static environment using two-dimensional ultrasound images," *Int. J. Robot. Res.* **33**(10), 1361–1374 (2014).
26. T. K. Adebar, A. E. Fletcher and A. M. Okamura, "3-D ultrasound-guided robotic needle steering in biological tissue," *IEEE Trans. Biomed. Eng.* **61**(12), 2899–2910 (2014).
27. X. Zhao, H. Guo, D. Ye and B. Huo, "Comparison of Estimation and Control Methods for Flexible Needle in 2D," *2016 Chinese Control and Decision Conference* (2016) pp. 5444–5449.
28. V. Duindam, R. Alterovitz, S. Sastry and K. Goldberg, "Screw-Based Motion Planning for Bevel-Tip Flexible Needles in 3D Environments with Obstacles," *IEEE International Conference on Robotics and Automation* (2008) pp. 2483–2488.
29. Z. Zhang, "A flexible new technique for camera calibration," *Tpami* **22**(11), 1330–1334 (2000).
30. J. Swensen, M. Lin, A. Okamura and N. Cowan, "Torsional dynamics of steerable needles: Modeling and fluoroscopic guidance," *IEEE Trans. Biomed. Eng.* **61**(11), 2707–2717 (2014).